




# Towards inhibiting conductivity of Mo/PVDF composites through building MoO<sub>3</sub> shell as an interlayer for enhanced dielectric properties

Weiwei Peng<sup>1</sup>, Wenying Zhou<sup>1,\*</sup> , Ting Li<sup>1</sup>, Juanjuan Zhou<sup>1</sup>, Tian Yao<sup>1</sup>, Hongju Wu<sup>1</sup>, Xueting Zhao<sup>1</sup>, Jin Luo<sup>1</sup>, Jiaxin Liu<sup>1</sup>, and Dongli Zhang<sup>2,\*</sup>

<sup>1</sup>School of Chemistry and Chemical Engineering, Xi'an University of Science & Technology, Xi'an 710054, China

<sup>2</sup>Academy of Agricultural Planning and Engineering, Key Laboratory of Technologies and Models for Cyclic Utilization From Agricultural Resources, Ministry of Agriculture, Beijing 100125, China

Received: 4 January 2022

Accepted: 5 May 2022

Published online:

26 May 2022

© The Author(s), under exclusive licence to Springer Science+Business Media, LLC, part of Springer Nature 2022

## ABSTRACT

Polymer dielectrics have received increasing attention owing to their wide applications in electrical, microelectronic and energy storage fields. However, it remains a challenging to prepare polymer dielectrics with a high dielectric constant ( $\epsilon$ ) but low dissipation factor ( $\tan\delta$ ). In this work, conductive molybdenum (Mo) particles were encapsulated by a thin layer of semi-conductive molybdenum trioxide (MoO<sub>3</sub>) with a wide bandgap of 3.28 eV via a facile thermal calcination way under air, and the gained core-shell structured Mo@MoO<sub>3</sub> particles were composited with poly(vinylidene fluoride) (PVDF) to generate morphology-controllable high- $\epsilon$  but low loss composites. The large  $\epsilon$  can be realized in the PVDF composites with the Mo@MoO<sub>3</sub>, and both the electric conductivity and  $\tan\delta$  of the composites are significantly restrained to rather low levels even at high filler loadings, and apparently decrease with increasing the MoO<sub>3</sub>' shell thickness. The significantly ameliorated dielectric performances can be ascribed to the presence of MoO<sub>3</sub> interlayer preventing the Mo particles from direct contact with each other and simultaneously hindering the long-range electron migration. The developed Mo@MoO<sub>3</sub>/PVDF composites with a high  $\epsilon$  but low loss are great potential applications for electrical industries and microelectronic industries.

## 1 Introduction

With the quick development of microelectronic devices towards large power, ultrahigh integration, ultrahigh-frequency, multifunction, and light weight,

dielectric materials with good overall performances such as high dielectric permittivity ( $\epsilon$ ), low dissipation factor ( $\tan\delta$ ) and high reliability are highly desired and essential for microelectronic device and electrical equipment such as embedded film capacitors in microelectronics, dielectric antenna and

Address correspondence to E-mail: wyzhou2004@163.com; dongliustb@126.com

electromagnetic interference shielding [1–4]. Compared with the traditional high- $\epsilon$  inorganic materials such as sodium bismuth titanate ( $\text{Ba}_x\text{Na}_{(1-x)}\text{TiO}_3$ , BNT), potassium tantalite–niobate ( $\text{KTa}_{(1-x)}\text{Nb}_x\text{O}_3$ , KTN), barium titanate ( $\text{BaTiO}_3$ ), copper calcium titanate (CCTO), etc., polymers have clear superiorities, including lightweight, excellent flexibility, easy process-ability and low cost, et al. [5–9]. Nevertheless, most of polymers always have very low  $\epsilon$  ( $\sim 10$ ) [10–12]. To solve this matter, some functional fillers with different types and shapes have been added into polymers to increase the  $\epsilon$  [3, 5–7]. Meanwhile, new challenges arise, i.e., as the volume fraction of filler increases, the dielectric loss, electrical resistivity and mechanical properties will decrease greatly [13–16]. Thus, the desirable polymeric dielectrics with high- $\epsilon$  but low loss and good mechanical properties can only be gained through combining the high-dielectric performances of fillers with polymers with prominent flexibility, very low loss and high breakdown strength by finely designing and controlling the adequate interfaces between the filler and matrix [3–6]. Therefore, the design and preparation of polymeric dielectrics with a high- $\epsilon$  but low loss has theoretical significance and engineering application values [1, 2, 5, 17–23].

Up to now, there are two relatively easy ways to fabricate high- $\epsilon$  polymer composites. One strategy is the organic/inorganic hybrid, that is to say, high- $\epsilon$  inorganic ferroelectric ceramics ( $\text{BaTiO}_3$ , BNT, monopotassium phosphate ( $\text{KH}_2\text{PO}_4$ ), etc.) are added into polymer matrix [1, 2, 8, 14–16, 24–28]. According to the mixing rules, usually a high filler loading (usually greater than 60 wt%) is required for a decent increase in the  $\epsilon$  of the composites, which inevitably deteriorates the electrical and mechanical properties of the composites [13, 18–25]. Another way to tackle this matter is to produce percolative composites, i.e., dispersing conductive fillers such as carbon materials like carbon black, carbon nano tube (CNT), graphite, metal particles (copper, zinc, nickel, etc.), etc., into insulator polymeric matrix [1, 13–16]. As the filler loading increases, the permittivity of composite dielectrics will remarkably rise at the percolation transition ( $f_c$ ) [3, 6–9, 15, 16, 29–34]. For example, only a small amount of conductive filler such as silver or CNT can lead to a large  $\epsilon$  in an insulator polymer thanks to the significantly enhanced interfacial polarization (IP) effect between the matrix and the filler resulting from the huge discrepancy in permittivity or conductivity

between the two components [18–22]. Thus, in this case, basing on percolative theory, the conductive fillers show a clear superiority over non-conductive inorganic fillers [2–4, 6, 8, 15, 16, 34]. Nevertheless, as the content of conductive fillers approaches the  $f_c$ , the percolation composites can harvest a very large  $\epsilon$ , but always suffer from a high  $\tan\delta$ , which significantly reduces the energy transformation and even challenges the long-term excellent stability of the associated microelectronic devices [13, 14, 21–25, 31]. The percolation transition appears a sharp exponential relationship with filler loading: at low filler,  $\epsilon$  increases slightly; on the contrary, at high filler content, an insulator-conductor transition happens, thereby leading to a conspicuous increase in both the  $\tan\delta$  and leakage current. Therefore, the microstructure and dielectric properties of percolation systems must be elaborately optimized to control the so-called “adjustable window” coming near the  $f_c$  [3, 6, 23–25, 32–35].

Nowadays, the construction of organic or inorganic insulating coating on the surface of conductive particles is able to act as an interlayer suppressing the transportation of free charge carriers between adjacent particles and inhibiting the formation of leakage current across the composites even at a high filler loading, and this is called a core–shell structured particles, becoming a crucial strategy to enhance the dielectric properties of percolating composites [10–12]. This kind of insulating organic or inorganic shells can be constructed either by complex chemical synthesis routes with high cost or by a facile and simple thermal oxidation method with simplicity and low cost [2, 15, 31]. For example, Li et al. grafted a thin layer of water-soluble amine functionalized polyethylene glycol monomethyl ether (PEG-NH<sub>2</sub>) onto graphene to obtain PEG-NH<sub>2</sub> functionalized graphene, and the introduction of the PEG-NH<sub>2</sub> interlayer not only strengthens the interfacial interactions between filler and epoxy, but also obviously restrains the loss and leakage current of composites [29]. Zhou et al. prepared core–shell structured Ni@NiO particles by directly calcining Ni powder at high temperature under air atmosphere, and compared with the virginal Ni/PVDF, the NiO shell not only enhances the IP effect resulting in improved permittivity in PVDF, but also remarkably restrains the loss due to its high electrical resistivity [34].

Molybdenum (Mo) is a well-known refractory metal with many excellent comprehensive properties,

such as, low expansion factor, high electric and heat conductivity, low resistivity and excellent structure stability, etc., which render it as a prospective candidate for the fabrication of percolation composites. Up to now, rare attention has been paid to the potential of Mo as filler for percolation composites. Like other metals or carbon materials, the Mo/polymer can show giant permittivity at the  $f_c$  due to IP effect, as well as large dielectric loss resulting from the formation of leakage current in the composites.

To effectively cope with this issue, in this work, we aim to construct a core-shell structured Mo particle via a simple thermal oxidation technology at high temperature under air atmosphere, and the morphology and shell thickness of the obtained Mo@MoO<sub>3</sub> (molybdenum trioxide) can be adjusted through changing the calcination conditions. Poly(vinylidene fluoride) (PVDF) was selected as the matrix in this work owing to its piezoelectric/ferroelectric properties with high  $\epsilon$  (about 10 at low frequencies) and high dielectric strength ( $E_b$ ,  $\sim 10^3$  kV/cm) and other favorable properties widely used to make high-energy-density dielectric materials [17, 23–25, 36]. It is well known that the MoO<sub>3</sub> is a semi-conductor with a wide bandgap of 3.28 eV, like traditional semi-conductors SiC and ZnO, which can restrain dielectric loss and leakage current, and effectively prevent surface flashover at high voltage. Thus, it was chosen as shell materials in this work. Moreover, the MoO<sub>3</sub> interlayer can effectively enhance the interfacial miscibility with the PVDF matrix through hydrogen-bond, hence improving the interfacial interaction between Mo and PVDF. Thus, this study is expected to understand the correlation between the microstructure and dielectric performances of composites for potential application in microelectronic and electrical industries.

## 2 Experimental

### 2.1 Materials

PVDF FR901 (99.9%, analytically pure (AR) grade) was purchased from 3F New Materials Co. (Shanghai, China). Molybdenum (labeled as Mo, 99.9%, AR grade) powders with a diameter of about 3–5  $\mu\text{m}$  were provided by Wuxi Shunda Metal Power Co. LTD). DMF (99.5%, AR grade) was bought from Tianjin Chemical Reagent Co. China.

### 2.2 Preparations

As shown in Fig. 1, the core-shell structured Mo@MoO<sub>3</sub> particles were prepared by calcining raw Mo powders under an air atmosphere in a furnace with different times and temperatures. The heat-treatment conditions for Mo particles were listed and numbered as below: Mo-1 (500 °C, 3 h), Mo-2 (550 °C, 1 h), Mo-3 (550 °C, 3 h) and Mo-4 (600 °C, 3 h), respectively.

Pure PVDF and the PVDF filled by different contents (10, 20, 30, 40, 50 and 60 wt%) of raw Mo or Mo@MoO<sub>3</sub> were prepared via a solution blending followed with hot-pressing technology. A certain quantity of PVDF was first dissolved in 10 mL DMF solvent by rapid stirring in 60 °C until the formation of homogeneous solution A. At the same time, a desirable number of fillers like raw Mo or Mo@MoO<sub>3</sub> particles were dispersed in 30 mL DMF with sonication for 15–20 min to form suspension B. Subsequently, the solution A and the suspension B were mixed and treated 12 h of agitation at room temperature, followed by casting and evaporating the majority of DMF at 100–110 °C in an oven. After that, the residual solvent was further removed from the samples at 120 °C in a vacuum oven. Finally, the composite was hot compressed at 190 °C for 10–15 min under a pressure of  $\sim 10$  MPa.

### 2.3 Characterizations

Fourier transform infrared (FT-IR) spectrometer (Perkin-Elmer, Paragon1000) was used to measure the surface chemistry of the samples over a spectrum range of 4000–400  $\text{cm}^{-1}$ .

The structures of the raw Mo and the Mo@MoO<sub>3</sub> particles were measured with Shimadzu XRD-6000 (XRD) equipped with a graphite monochromatic instrument and a Cu anticathode (40 kV, 30 mA, scanning rate 2°/min).

A JEOL JSM-7000F scanning electron microscope (SEM) was used to survey the fracture morphology of specimen. First, the composites need to be fractured in liquid nitrogen, and then the fractured surface was sprayed with a layer of gold in vacuum before observation. And the SEM was equipped with energy dispersive spectroscopy (EDS). The microstructure of the raw Mo and Mo@MoO<sub>3</sub> particles was inspected with an H-800 transmission electron microscope (TEM) from Hitachi Co (Japan).

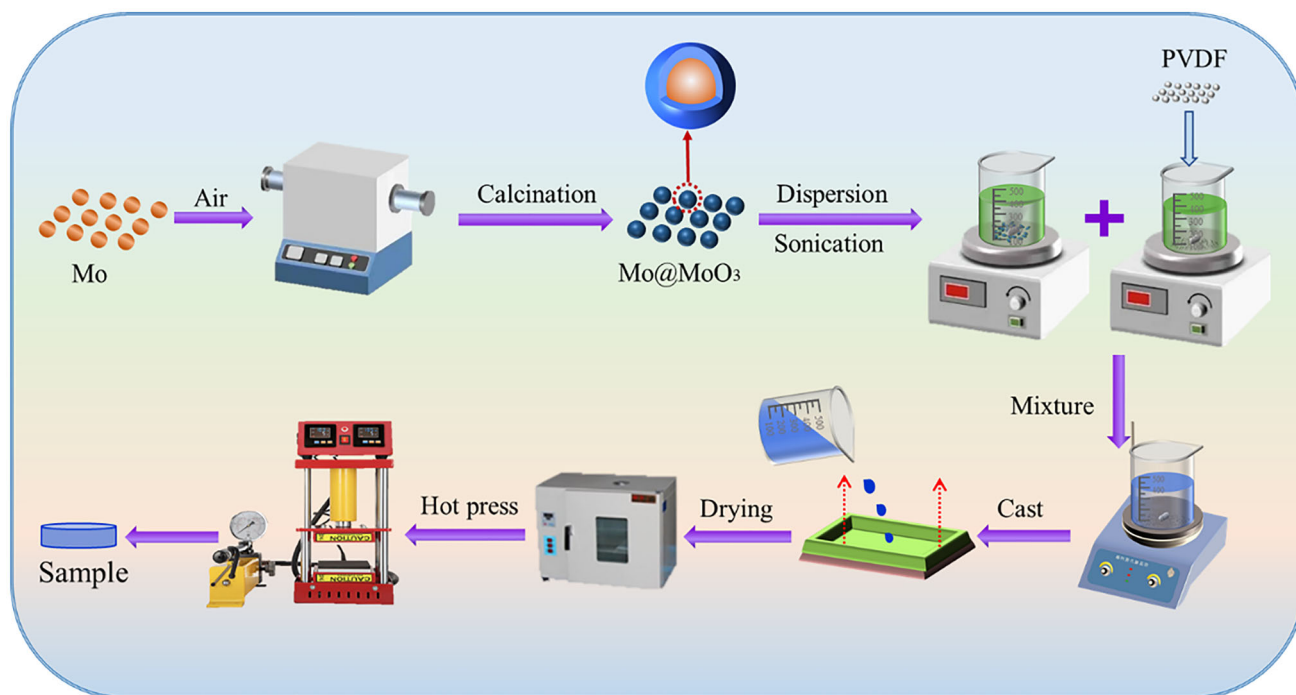


**Fig. 1** The schematic showing the preparation of the Mo@MoO<sub>3</sub> and corresponding PVDF composites

Sample weight loss upon heating was carried out through a Thermogravimetric analysis-differential scanning calorimetry (TG-DSC, SDTA851, Swiss) measurements. Measurement temperature under an air atmosphere from room temperature to 600 °C at a heating rate of 10 °C/min.

The dielectric properties of the samples were examined by an Agilent 4294 A impedance analyzer over a frequency range 40 Hz to 10<sup>7</sup> Hz at room temperature.

### 3 Results and discussion

#### 3.1 Characterizations of core-shell Mo@MoO<sub>3</sub> particles

To determine the microstructure of the obtained MoO<sub>3</sub> shell on the surface of raw Mo particle, a series of characterizations were performed, and the consequences are presented in Fig. 2 and Table 1. Figure 2a demonstrates the XRD patterns for raw Mo and Mo@MoO<sub>3</sub> particles. The peaks at  $2\theta = 40.1^\circ$ ,  $58.6^\circ$ ,  $73.7^\circ$  and  $87.6^\circ$  are indexed to the diffraction planes of (110), (200), (211) and (220) from crystalline Mo, respectively, indicating the cubic phase of metallic Mo (JCPDS card no.42-1120). Compared with the raw

Mo, new intensity peaks at  $2\theta = 12.4^\circ$ ,  $23.0^\circ$ ,  $25.4^\circ$ ,  $27.0^\circ$ ,  $29.3^\circ$ ,  $33.4^\circ$ ,  $39.2^\circ$ ,  $45.4^\circ$ ,  $46.1^\circ$ ,  $49.0^\circ$ ,  $52.5^\circ$ ,  $54.7^\circ$ ,  $56.0^\circ$ ,  $62.9^\circ$ ,  $64.8^\circ$ ,  $69.26^\circ$ ,  $78.67^\circ$  and  $81.11^\circ$  are belonging to the (200), (101), (400), (011), (111), (600), (003), (511), (020), (402), (420), (212), (412), (521), (122), (114), (311) and (031) crystal planes of MoO<sub>3</sub>, respectively. It is worth noting that the peak intensity near (011) plane is visibly increased with an increase in the calcined temperature, which is a small intensity peak in monoclinic MoO<sub>3</sub>. From the above discussion, the conclusion can be reached that the MoO<sub>3</sub> is formed on the surface of Mo particle. In addition, based on Debye–Scherrer’s equation and Bragg equations, the formation of MoO<sub>3</sub> on the surface of Mo would change the average crystallite size of the original Mo, which is shown in Tab. S1. From the Fig. S1 and Tab. S1, it is clearly seen that the crystal plane spacing are basically the same as the JCPDS card. Thus, the obtained MoO<sub>3</sub> shell retained the complete crystallinity still and not destroyed the crystal structure of Mo, also plays an important impact on the dielectric properties of Mo/polymer composites.

Figure 2b displays the FT-IR spectra of the Mo particles before and after calcination. The absorption bands of the H<sub>2</sub>O appear at about  $3450\text{ cm}^{-1}$  and  $1610\text{ cm}^{-1}$ , respectively, which correspond to the characteristic peaks for the hydroxyl groups (OH<sup>-</sup>) in

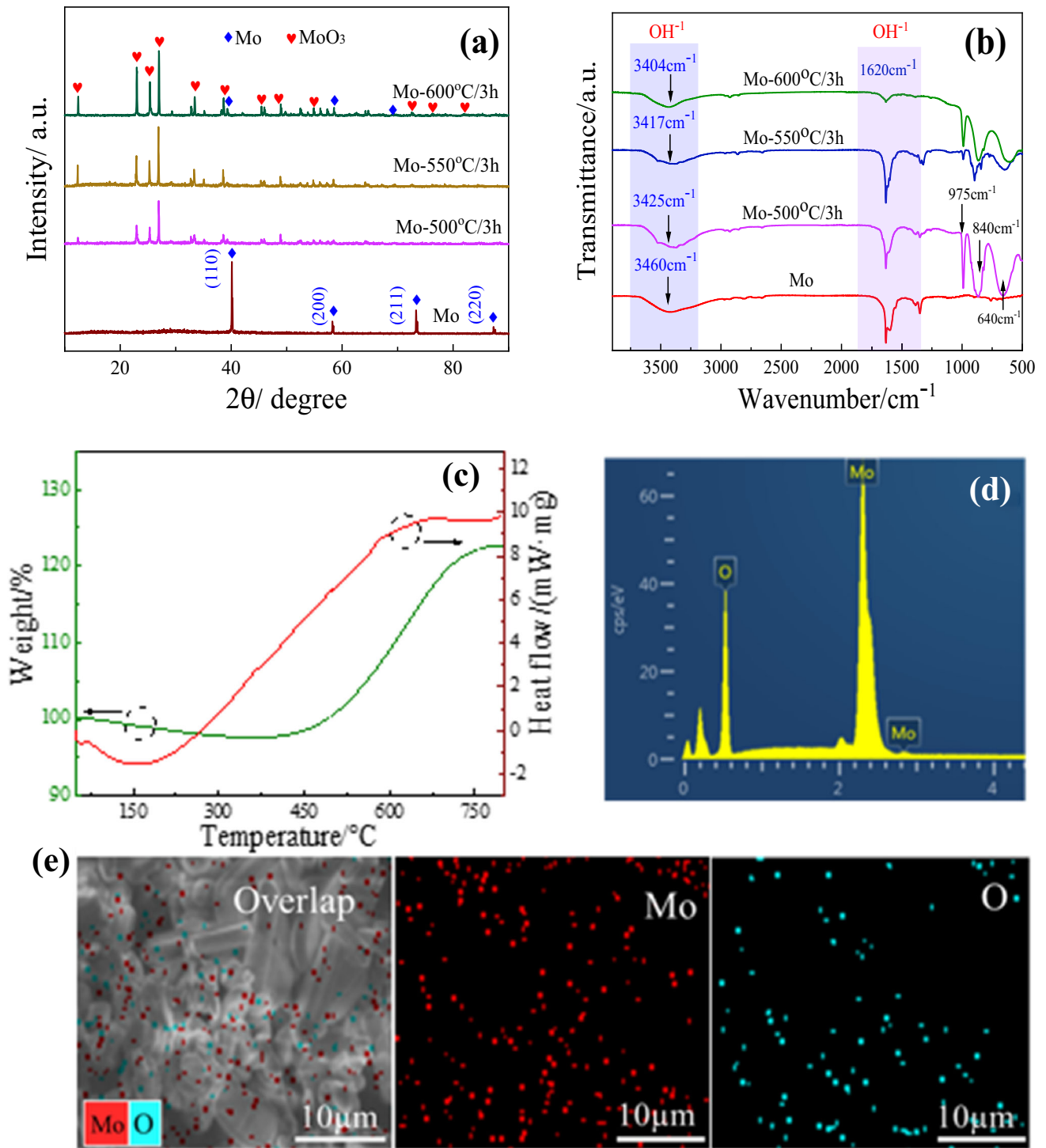


**Fig. 2** a XRD, b FT-IR for Mo particles without and with calcination, c TG-DSC for Mo particles, d EDS for MoO<sub>3</sub> particles, e EDS element mapping of the calcinated MoO<sub>3</sub> particles

the two filler particles [4, 8, 11, 12]. Surprisingly, the absorption band becomes wide and leans to a smaller wave number at about 3200–3600 cm<sup>-1</sup>. Hence, this phenomenon also proves the formation of the

intermolecular hydrogen bonding. Compared to raw Mo particles, the asymmetric absorption peaks at 585 cm<sup>-1</sup>, 870 cm<sup>-1</sup> and 975 cm<sup>-1</sup>, respectively, refer to the stretching vibration of Mo=O bond in the

**Table 1** The assignment of the showed bands of FT-IR for the Mo and MoO<sub>3</sub> particles

Attributed to <sup>a</sup>	Mo	MoO <sub>3</sub>
$\nu_{\text{OH}}$	3460	3425, 3417, 3404
$\delta_{\text{OH}}$	1630	1628, 1625, 1620
$\nu_{\text{M=O}}$	No	970, 840, 640
References	[3, 4, 6, 9]	[4, 11, 35]

<sup>a</sup> $\nu$  Stretching;  $\delta$  bending

calcined Mo particles, which also directly explains that the MoO<sub>3</sub> has been coated around the outside surface of pristine Mo.

Figure 2c presents the TG-DSC measurements curves of the Mo particles heated from 30 to 800 °C under air. There are two major weight loss phases in the TGA curve. Firstly, an apparent weight loss appears below 300 °C because the moisture and other small molecules physically absorbed on the surface of the particles are evaporated, which is described on an endothermic peak in the DSC curve near 100 °C. Afterwards, the Mo particles are gradually oxidized in this range of 400–650 °C, the sharp weight increase starts at about 550 °C and becomes steady at 680 °C, corresponding to an exothermic peak in the DSC curve at 680 °C. After that, almost no weight variation can be noticed because of the excellent thermal stability of the oxide. The TGA results further reveal the formation of MoO<sub>3</sub> shell on the surface of raw Mo after calcination at high temperature.

EDS analysis was employed to study the elements distribution of calcined Mo particles, as seen from Fig. 2d–e. Obviously, the EDS images manifest that the surface of samples consists of Mo and O elements, which is consistent with the consequences from FT-IR and XRD analysis. Of course, the uniformly distributed O element indicates the formation of a homogeneous MoO<sub>3</sub> shell on the surface of Mo particles. The successfully coated MoO<sub>3</sub> shell not only modifies the electrical properties of Mo, as an interlayer, but also plays a prominent role in the mechanical, dielectric and other properties of the Mo/polymer composites.

### 3.2 Microstructures

Figure 3 displays the TEM images of raw Mo and Mo particles calcined at 500 °C for 3 h and 600 °C for 3 h, respectively. As shown in Fig. 3a and Fig. 3d, no

noticeable external layer can be seen for the raw Mo particles, whereas, it can be clearly observed from Fig. 3b–c that a layer of MoO<sub>3</sub> shell was constructed on the external surface of the raw Mo, and the shell thickness increases with calcination temperature. Moreover, from the high-resolution TEM images in Fig. 3d–f, spaced parallel strips, i.e., lattice fringe, can be clearly substantiated in the calcined Mo particles in direct contrast to the raw Mo as indicated in Fig. 3d. Through Digital Micrograph software, the crystal spacing for Mo and Mo@Mo<sub>3</sub> can be demarcated easily. It is clearly that the pattern shows the distinct lattice fringes with a spacing of 1.11 Å and 1.28 Å for the (220) and (211) plane of Mo particles, respectively. And the distinct lattice fringes with a spacing of 3.06 Å and 2.29 Å, correspond to the two facets of (101) and (003) of MoO<sub>3</sub>, respectively. And the Fast Fourier Transform (FFT) also confirms the formation of MoO<sub>3</sub> lattice plane. Thus, the obtained MoO<sub>3</sub> shell retained the complete crystallinity still, revealing a well-ordered crystal structure. This is direct evidence for the crystalline structured MoO<sub>3</sub> formed during calcination, which conforms to the consequences from the XRD measurements.

Figure 4 gives the SEM images of raw Mo, Mo@MoO<sub>3</sub> and their PVDF-based composites at different filler loadings. As illustrated in Fig. 4a–b, the diameter of raw Mo specimens is about 3–4 µm in average, and the surface of Mo particles is a little smooth. After calcination, the Mo@MoO<sub>3</sub> still remain the same shape and diameter due to ultrahigh softening point and melting point. Thus, as indicated in Fig. 3, just a nanoscale thin shell oxide was formed outside the pristine Mo during the oxidation process. From Fig. 4c–d, the raw Mo particles are dispersed irregularly in the PVDF matrix with obvious aggregation because of weak interfacial interactions between the filler particles and the matrix. However, it is found that the Mo@MoO<sub>3</sub> particles are more evenly dispersed in the PVDF, as shown in Fig. 4e–i, which is attributed to enhanced interfacial interactions between the fillers and the matrix. Compared with the raw Mo, the more numbers of hydroxyl groups have been generated on the surface of Mo during high-temperature calcination. Thus, the hydroxyl groups in the Mo@MoO<sub>3</sub> particles can form hydrogen bond with the F atom in the PVDF, which makes the fillers more homogeneous dispersion in the matrix through strengthening the interfacial compatibility and interactions between the two

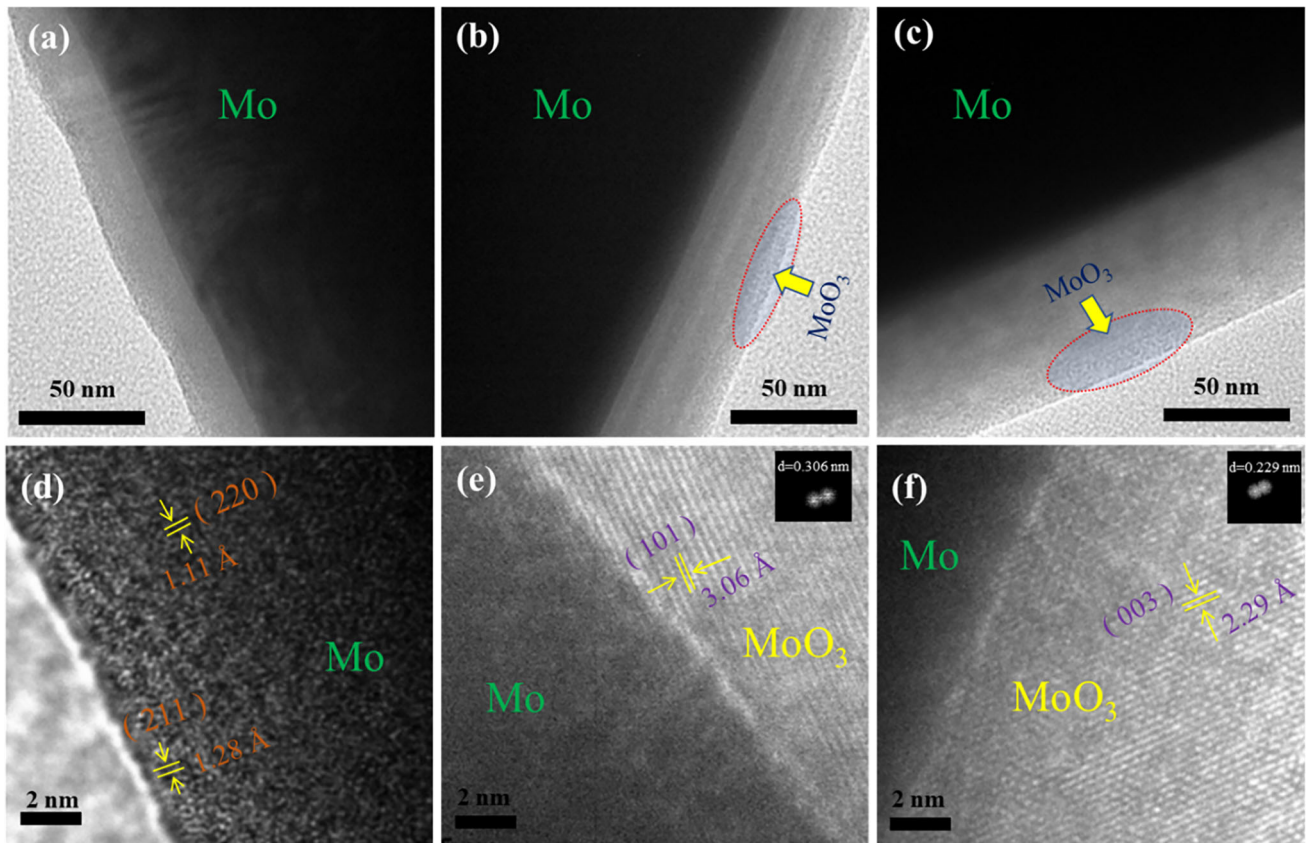


**Fig. 3** TEM images of **a, d** pure Mo, **b, e** Mo calcinated at 500 °C for 3 h, and **c, f** Mo calcinated at 600 °C for 3 h

components, as illustrated in Fig. 8. Thus, the presence of the MoO<sub>3</sub> interlayer will impart the composites' better physical properties by enhancing interfacial interactions, compared with pristine Mo/PVDF with weak interfacial interactions.

### 3.3 Dielectric properties

Figure 5a–e displays the variation of  $\epsilon$  with filler loading and frequency for the PVDF composites with Mo and Mo@MoO<sub>3</sub>. The  $\epsilon$  of composites demonstrates a positive correlation with the filler loading. The more number the filler particles are in the composites, the larger the  $\epsilon$  is. When the filler loading is less than 30 wt%, the  $\epsilon$  of original Mo/PVDF and Mo@MoO<sub>3</sub>/PVDF composites have no evident changes with frequency because a small amount filler particle is insufficient to constitute enough micro capacitor and the dielectric behavior of composites is mainly derived from the PVDF polarizations. Therefore, the use of fillers only offers an insignificant enhancement in  $\epsilon$  [18–22]. When the filler concentration is more than 30 wt%, a forceful frequency

dependence of  $\epsilon$  is more prominent in the frequency range from 40 to 10<sup>5</sup> Hz, which roots in the IP effect arisen by the possible impurity and defects and micro capacitance model coming from adjacent conductive particles as electrode [3, 31–34]. And a sharp decline tendency in  $\epsilon$  arises in the frequency of 10<sup>5</sup> to 10<sup>7</sup> Hz due to the PVDF dipole relaxation moments.

As illustrated in Fig. 5a, the  $\epsilon$  of Mo/PVDF is obviously larger than that of pure PVDF. For instance, at 40 wt%, the  $\epsilon$  of Mo/PVDF is nearly 200 at 100 Hz, but the  $\epsilon$  of pure PVDF is 10. Such remarkable enhancement in  $\epsilon$  can be interpreted based on the fact that the conductive Mo particle possesses a high conductivity compared with the insulating PVDF matrix, which makes the interface between Mo and PVDF gathered a good deal of charge carriers working as electron dipoles to improve the composites polarization effect. To be specific, the effect above is also closely connected to the filler concentration. When the filler loading is less than 30 wt%, the  $\epsilon$  of composites increases slightly and nearly linearly rises with the Mo content because a handful of Mo particle are separated so far away

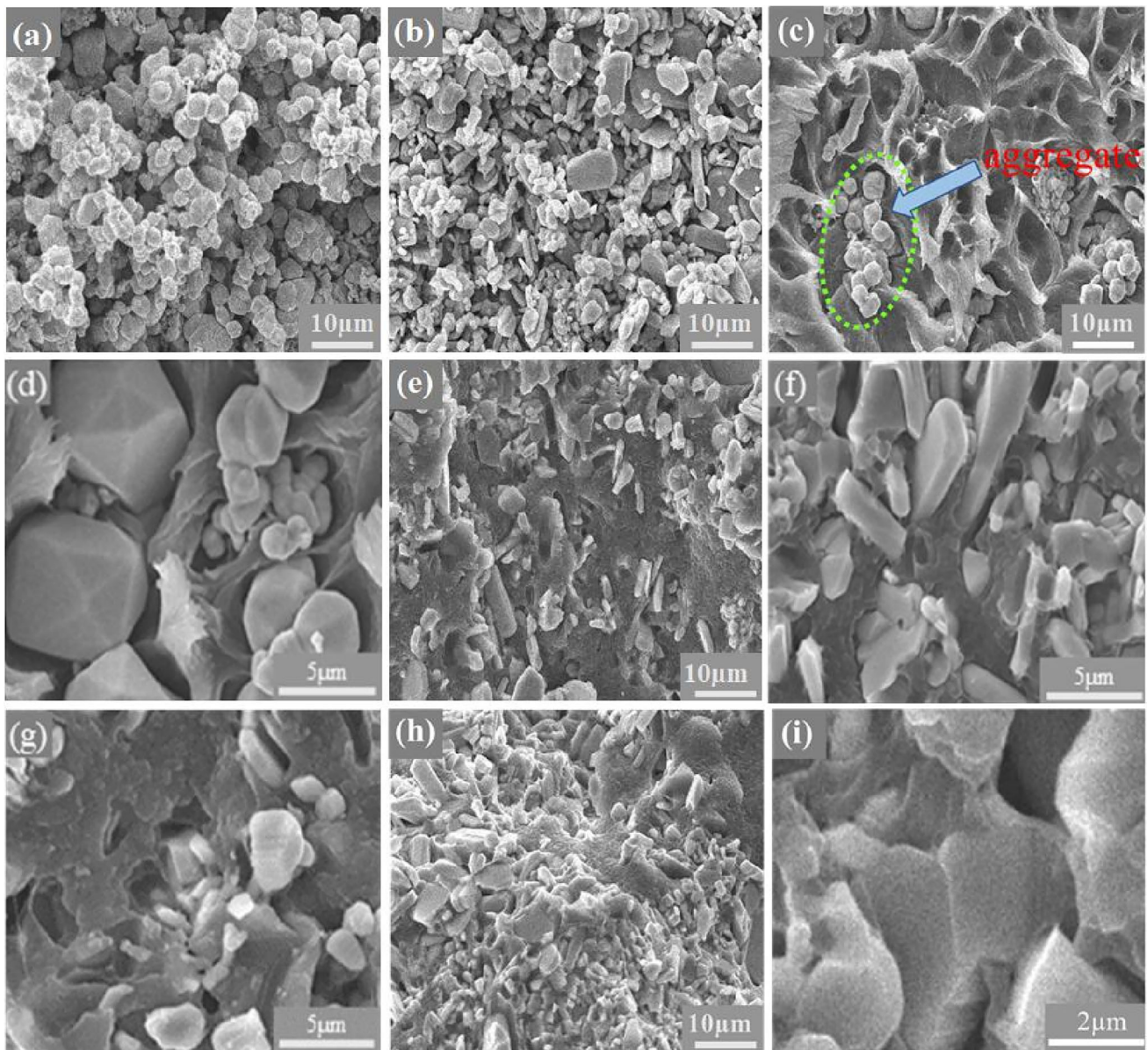


**Fig. 4** SEM images for **a** raw Mo, **b** Mo-1, **c–d** 40 wt% raw Mo/PVDF, **e–f** 40 wt% Mo-1/PVDF, **g** 40 wt% Mo-3/PVDF, and **h–i** 60 wt% Mo-3/PVDF

from each other, thus resulting in low electron polarization. When the filler loading is close to the  $f_c$ , a drastic enhancement in  $\epsilon$  is attributed to the direct contact with each other of Mo particles and lot of charge carriers are trapped at the interface between polymer and filler, facilitating a massive acceleration in the number of micro capacitors and the extent of IP [11, 32–34]. Moreover, with increasing the filler concentration of Mo > 30 wt%, the  $\epsilon$  arises exponentially, suggesting the formation of the percolated paths and the transition from insulator to conductor. When the electrons are capable of tunneling/hopping across

several neighboring conductor Mo particles, the charge separation can be conspicuously enhanced and the  $\epsilon$  will present the sharp variations.

The  $\epsilon$  of a composite can be explained by the power law:

$$\epsilon = \epsilon_m (f_c - f)^{-s} \quad (1)$$

where,  $\epsilon_m$  is the  $\epsilon$  of the matrix,  $f$  is the filler volume fraction, and  $s$  is an exponent of about 1. As demonstrated in Fig. 5f, the best fit of the  $\epsilon$  of Mo/PVDF gives an  $f_c \approx 10.61$  vol% (about 40 wt%) and  $s \approx 0.70$ .



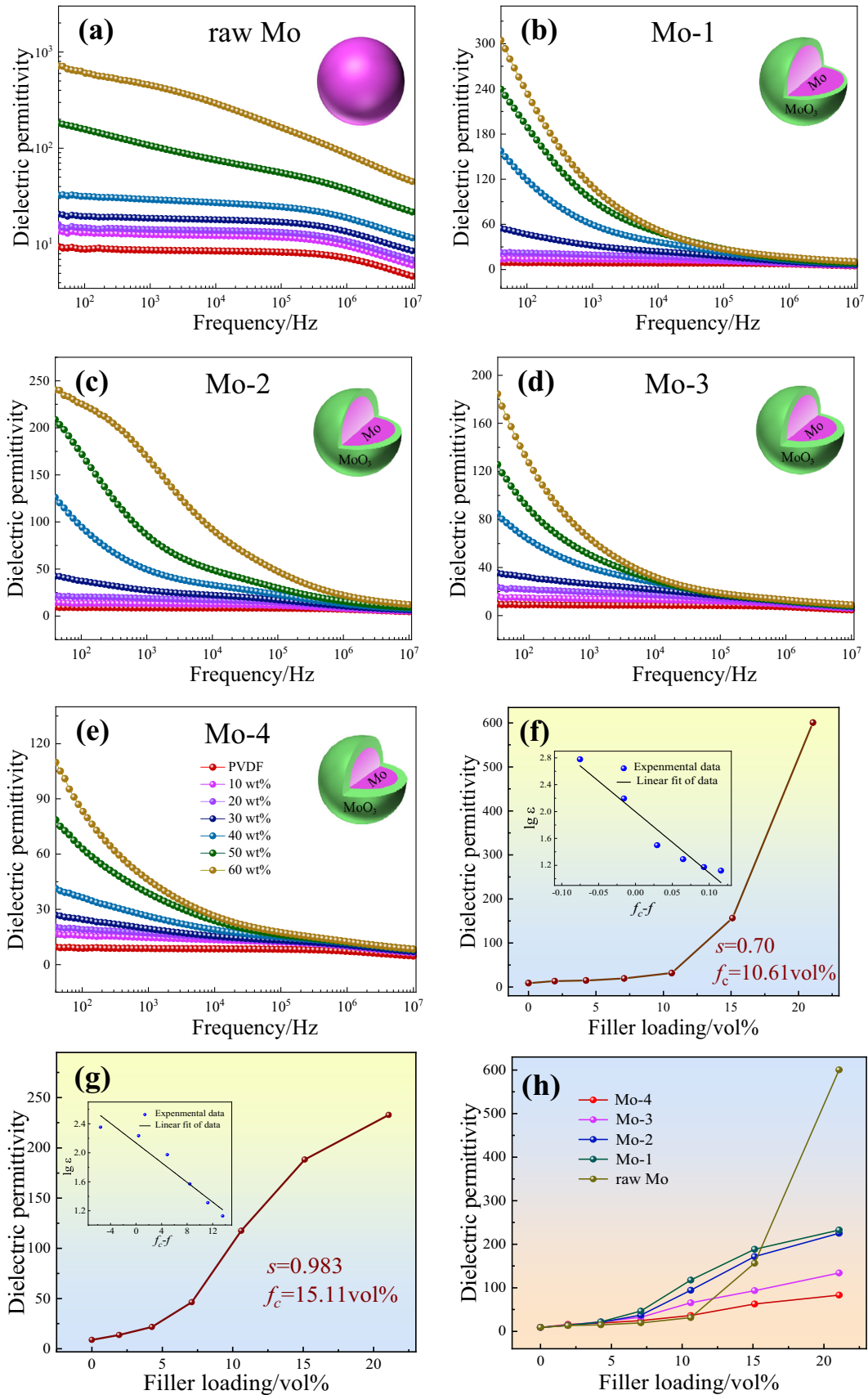


**Fig. 5**  $\epsilon$  dependence on frequency and filler loading for the PVDF filled with: **a** raw Mo, **b** Mo-1, **c** Mo-2, **d** Mo-3, and **e** Mo-4; **f**, **g**  $\epsilon$  of raw Mo particle and Mo-1 as a function filler loading at 100 Hz, the inset presenting a log–log plot of  $\epsilon$  vs.  $(f_c - f)$ , **h**  $\epsilon$  of PVDF composites (100 Hz) with different loading of raw Mo and various Mo@MoO<sub>3</sub>

Figure 5b–e provides the dependence of  $\epsilon$  on the filler loading and frequency for the calcined Mo/PVDF composites. Compared with the raw Mo/PVDF, the Mo@MoO<sub>3</sub>/PVDF composites present visibly lower  $\epsilon$  but they are still much higher than that of pure PVDF. For example, when filler loading is 60 wt%, the  $\epsilon$  at 100 Hz is 600.6 (raw Mo/PVDF), 232.73 (Mo-1/PVDF), 225.1 (Mo-2/PVDF), 133.99 (Mo-3/PVDF), 83.1 (Mo-4/PVDF) and 8.9 (pure PVDF), respectively. It is considered that the semi-conductor MoO<sub>3</sub> interlayer acts as a passivation shell on the surface of the Mo core, which not only available hinders charge transportation between the Mo particles and restricts charge displacement, but also effectively alleviates space charge polarization due to a reduction in the number of traps, thus causing an obvious decrease in  $\epsilon$  for Mo@MoO<sub>3</sub>/PVDF composites. In addition, combination with SEM and XRD results, the Mo@MoO<sub>3</sub> particles exhibit good homogeneous dispersion in PVDF, resulting in fewer defects in the system, which contributes to the slight improvement of  $\epsilon$  for Mo@MoO<sub>3</sub>/PVDF composites.

As demonstrated in Fig. 5f, the best fit of the  $\epsilon$  of Mo@MoO<sub>3</sub>/PVDF receives an  $f_c$  of 15.11 vol% (about 50 wt%) and  $s$  of 0.983, respectively. Clearly, the formation of the semi-conductor MoO<sub>3</sub> shell on the outside of the Mo particles promotes the  $f_c$  to shift towards a greater concentration. As expected, the appearance of percolation transition is perceptibly delayed, and can only be triggered at a much higher concentration, thus increasing the electrical resistivity of composites through inhibiting the conductivity of filler and composites. In order to uncover the effect of the MoO<sub>3</sub> shell on the  $\epsilon$ , the  $\epsilon$  of PVDF with pristine Mo and calcined Mo with four different shell thicknesses was also compared in Fig. 5h. According to Fig. 3b–c, e–f, the higher the calcination temperature is, the thicker the MoO<sub>3</sub> shell is, as indicated in the Tem images in Fig. 3 that is to say, the  $\epsilon$  for the composites researched here first keeps on increasing as the MoO<sub>3</sub> shell thickness increases on account of the gradually improved interface compatibility and

the contribution from the new formed interface between Mo and PVDF, thereby facilitating the enhancement of IP, followed by a consecutive but mild reduction in  $\epsilon$  because further thickening the MoO<sub>3</sub> shell would reduce the possibility of electron tunneling and hopping through the shell [3, 6, 32–34]. What is noteworthy is that the Mo-1 particles endow the PVDF with the highest  $\epsilon$  at low frequencies compared with Mo particles fabricated under other calcination conditions, indicating that the IP can be induced to an optimal level by changing the calcination conditions to optimize the thickness of the MoO<sub>3</sub> shell for best dielectric performances [23–25].

Figure 6 shows the dependence of  $\tan\delta$  as a function of frequency and filler loading for Mo/PVDF and Mo@MoO<sub>3</sub>/PVDF. Generally, the  $\tan\delta$  is regarded as the sum of electrical leakage loss and polarization loss in the whole frequency range. In total, it is clear that the  $\tan\delta$  of all composites rises with an increase in filler loading, especially for the raw Mo/PVDF. At an  $f < f_c$ , the filler particles are distanced from each other, whereas, when the filler loading is more than  $f_c$ , the direct current (DC) conduction is observed thanks to the formation of conductive network across the composites. What is especially fascinating is that there are two different peaks in the loss curve. The first peak at low frequency (40–10<sup>4</sup>) derives from the electric leakage of the conductor Mo particles and the dielectric response of enhanced interfacial relaxation as well as space charges or imperfections. The second peak at high frequency is owing to the dipole orientation polarizations of C–F from the PVDF matrix which contributes to the formation of the Debye relaxation behavior [10, 12, 31].

As shown in Fig. 6a, evidently, the  $\tan\delta$  of the Mo/PVDF composites increases with increasing the Mo loading. When the Mo loading is lower than  $f_c$ , the variation in loss is almost independency of filler concentration and the  $\tan\delta$  stays at a rather lower level because the neighbor particles are ultimately isolated from far away with each other. While, once the Mo loading is beyond the  $f_c$ , the  $\tan\delta$  increases sharply to quite a high level. The large  $\tan\delta$  at low frequency is mainly due to the DC conduction from the formation of quasi-conductive network of Mo filler contacting with each other, greatly contributing to the dielectric loss according to Eqs. (2–3). Figure 6b–g shows the variation in  $\tan\delta$  for the PVDF reinforced with Mo particles calcined at different calcination conditions. Compared with Mo/PVDF,

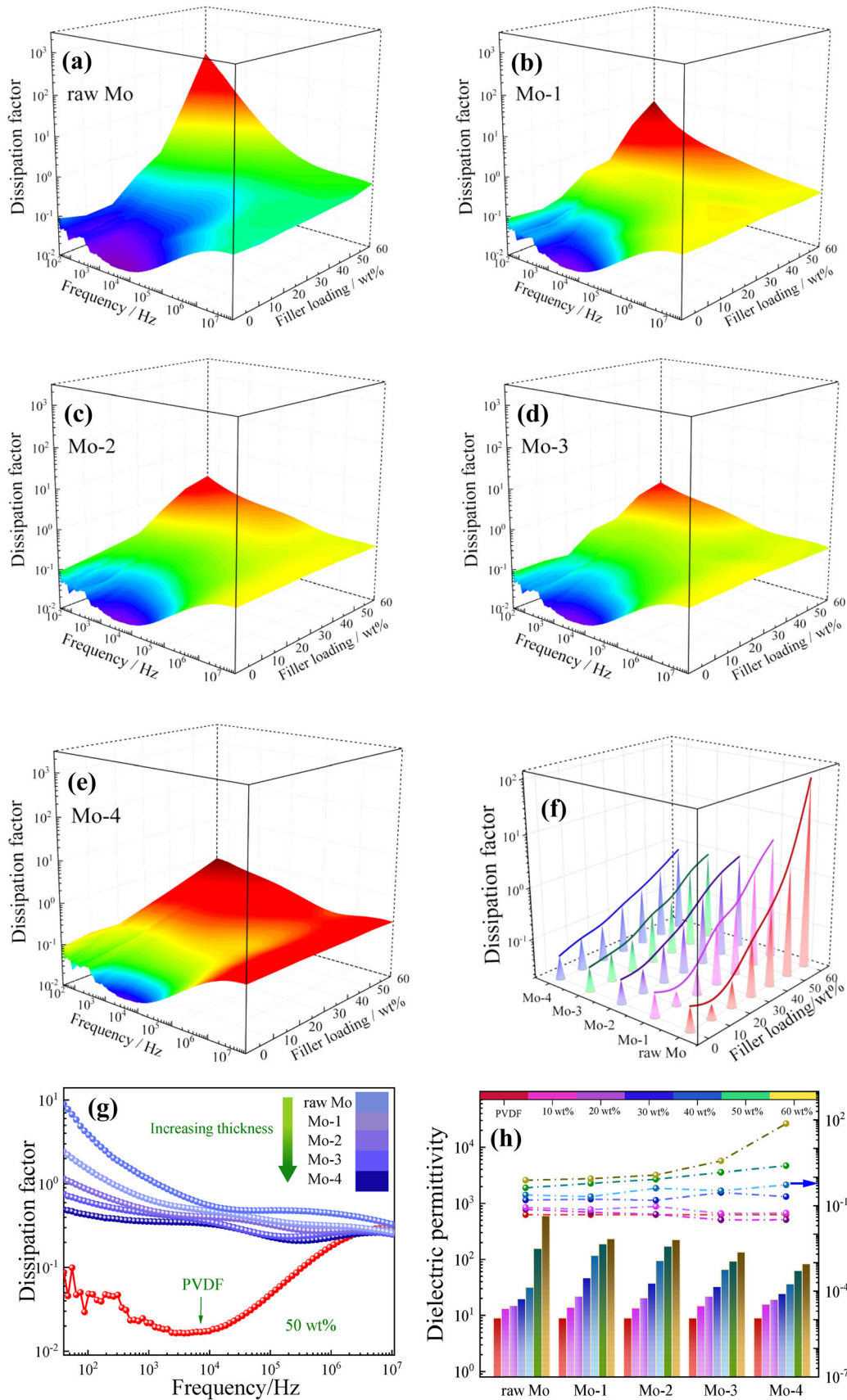


**Fig. 6**  $\tan\delta$  of PVDF composites as a function of filler loading and frequency: **a** raw Mo, **b** Mo-1, **c** Mo-2, **d** Mo-3, and **e** Mo-4. **f**  $\tan\delta$  of PVDF composites with raw Mo and various Mo@MoO<sub>3</sub> at 100 Hz. **g**  $\tan\delta$  v.s. frequency for PVDF at 50 wt% of fillers. **h**  $\epsilon$  and  $\tan\delta$  of composites with different loading of Mo and Mo@MoO<sub>3</sub> at 100 Hz

the  $\tan\delta$  of Mo@MoO<sub>3</sub>/PVDF is retained at a remarkably lower level, and almost no percolation behavior can be observed before the Mo@MoO<sub>3</sub> loading approaches to 50 wt%. This is probably due to the presence of semi-conductive MoO<sub>3</sub> shell that prevents the Mo fillers from coming into contact with each other and generating leakage current across the composites. As a result, the migration of free charge carriers can be significantly restrained and limited, thus lessening the leakage current and the resulting dielectric loss.

To further analyze the influence of the thickness of MoO<sub>3</sub> shell on suppressing the  $\tan\delta$  of the composites, the  $\tan\delta$  of Mo/PVDF and four types of Mo@MoO<sub>3</sub>/PVDF are also compared in Fig. 6f. The loss curves of Mo@MoO<sub>3</sub>/PVDF show almost similar trends as those of the Mo/PVDF composites aside from the cases with high filler loading. For the  $\tan\delta$  of Mo@MoO<sub>3</sub>/PVDF, nearly no percolation behavior can be noticed even at a filler loading greater than the  $f_c$ , manifesting the effective suppression of the crystalline MoO<sub>3</sub> shell on the long-range migration of charge carriers because of its much high electrical resistivity. Furthermore, the thicker the MoO<sub>3</sub> shell is, the stronger the restraint on the long-range charges' migration is, because the thicker interlayer generates pronounced suppression on the leakage current of Mo, thereby obviously restraining the dielectric loss of composites. For example, when the filler loading is 60 wt%, the  $\tan\delta$  (100 Hz) of PVDF with Mo-1, Mo-2, Mo-3, and Mo-4, are 3.83, 1.19, 0.89 and 0.79, respectively, compared to 74.5 for the raw Mo/PVDF at the same filler loading, manifesting the significant inhibiting effect of the interlayer on the leakage current and loss of composites.

Generally, the following equation can be used to express the dielectric loss ( $\epsilon''$ ) of a composite:

$$\epsilon'' = \epsilon''_{dc} + \epsilon''_{MW} + \epsilon''_D \quad (2)$$

where  $\epsilon''_{dc}$  and  $\epsilon''_{MW}$  stand for the losses from conduction and IP, respectively, and  $\epsilon''_D$  relates with the dipole loss factor.

The conduction loss is expressed by:

$$\epsilon''_{dc} = \frac{\sigma_{dc}}{2\pi f} \quad (3)$$

where  $\epsilon''_{dc}$  and  $f$  stands for the DC conduction loss and frequency, respectively.

It is known that conduction loss is dominant in the low frequency range which could lead to a large. Based on Eqs. (2)–(3), in the total of Mo@MoO<sub>3</sub>/PVDF, there is almost no conduction loss appearing on account of the presence of the semi-conductor MoO<sub>3</sub> shell, which effectively frustrates the charge transfer and restrains the DC conductivity to very low levels thanks to its wide forbidden band, thus leading to significantly reduced  $\tan\delta$  of Mo@MoO<sub>3</sub>/PVDF composites, and this phenomenon is also confirmed in Fig. 6g. The  $\epsilon$  and  $\tan\delta$  of Mo/PVDF and Mo@MoO<sub>3</sub>/PVDF at 100 Hz are summarized in Fig. 6h, it can be found that the Mo-2/PVDF composite exhibits a comparably high  $\epsilon$  and very low  $\tan\delta$ . Therefore, in this work, the best filler chosen is the Mo-2 particles with overall super dielectric properties.

Figure 7 plots the variations of electric conductivity of the Mo/PVDF and Mo@MoO<sub>3</sub>/PVDF composites. Obviously, the alternating current (AC) conductivities of all composites exhibit the almost same tendency with frequency. For the raw Mo/PVDF composites shown in Fig. 7a-1, when the Mo loading is less than the  $f_c$ , the AC conductivity is seen to slowly rise with increasing the filler loading, attributive to the relatively homogeneous dispersion of a small amount of Mo in PVDF. When the filler loading is no less than the  $f_c$ , the Mo particles gradually start to directly contact each other and generate a conductive network in the composites. Thus, finally, the composites will change from an insulator to a conductor, which makes the DC conduction appear at low frequency with further increasing the filler loading. At this point, the electrical resistivity will descend severely.

From Fig. 7a-2-a-5, the AC conductivities are suppressed observably in all Mo@MoO<sub>3</sub>/PVDF composites at the entire frequency range, even if the filler loading is at high level much greater than the  $f_c$ . For comparison purpose, the electric conductivities of the composites are dramatically inferior to the raw Mo/PVDF composites. The AC conductivities of Mo@MoO<sub>3</sub>/PVDF composites slowly increase with

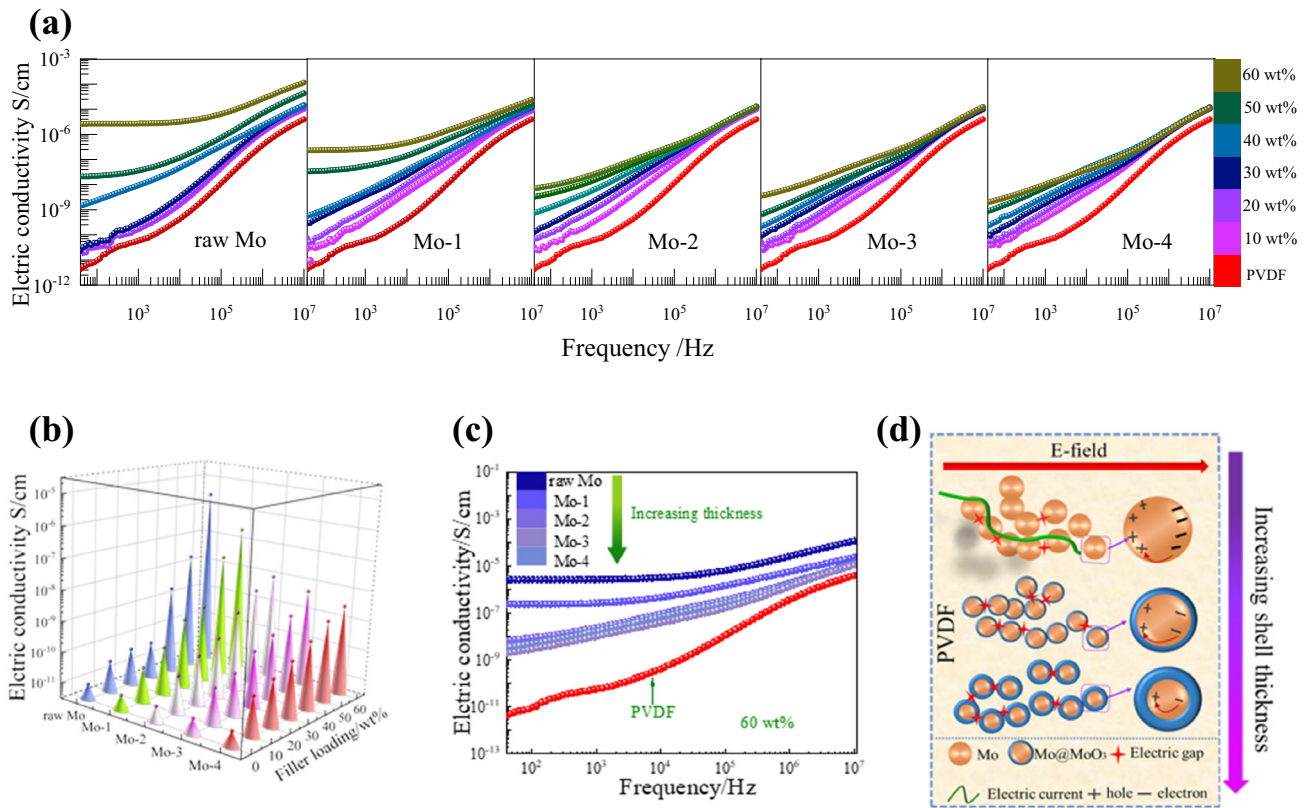


**Fig. 7** **a** Electric conductivity of PVDF composites as a function of frequency with different calcining times and temperatures, **b** electric conductivity of PVDF composites (100 Hz) with raw

increasing the filler loading, attributive to the step-by-step enhanced shell' prohibiting influence on the electron conduction and free carrier migration process. As illustrated in Fig. 7b, a gradual reduce in AC conductivity with the same filler loading is clearly observed due to the interlayer' increasing restraining effect on electron conduction process with increasing the thickness of semi-conductor MoO<sub>3</sub> layer. Besides, Fig. 7c illustrates the relationship between the AC conductivity and the MoO<sub>3</sub> shell thickness at a filler loading of 60 wt%. The electric conductivity values (1000 Hz) of composites are listed as the following order: raw Mo (2.60E<sup>-6</sup>), Mo-1 (2.33E<sup>-7</sup>), Mo-2 (9.03E<sup>-9</sup>), Mo-3 (5.07E<sup>-9</sup>) and Mo-4 (2.95E<sup>-9</sup>), respectively. It is clear that the AC conductivities are suppressed significantly to very low levels in all Mo@MoO<sub>3</sub>/PVDF composites compared with the raw Mo/PVDF, even at a filler loading much higher than the *f<sub>c</sub>*. The much-restrained conductivity can be ascribed to the crystalline MoO<sub>3</sub> interlayer with much high electrical resistivity, which greatly prevents the adjacent fillers from contacting with each other, thus

Mo and various Mo@MoO<sub>3</sub>, **c** frequency v.s. electric conductivity of composites at 60 wt% of filler, **d** effects of the MoO<sub>3</sub> shell and its thickness on electrical properties of composites

effectively impeding the formation of conductive network, and decreasing the conductivity through electron migration activation energy with increasing the thickness of MoO<sub>3</sub> [3, 6, 17, 32–34]. This suppression effect is demonstrated in Fig. 7d. So, in order to restrain the loss and AC conductivity of the composites, the semi-conductive crystalline interlayer' structures including the electrical resistivity, crystalline and thickness much be exquisitely designed and optimized for expected desirable dielectric properties for the core–shell structured particles and polymeric composites (Fig. 8).

### 3.4 Further understanding of dielectric properties

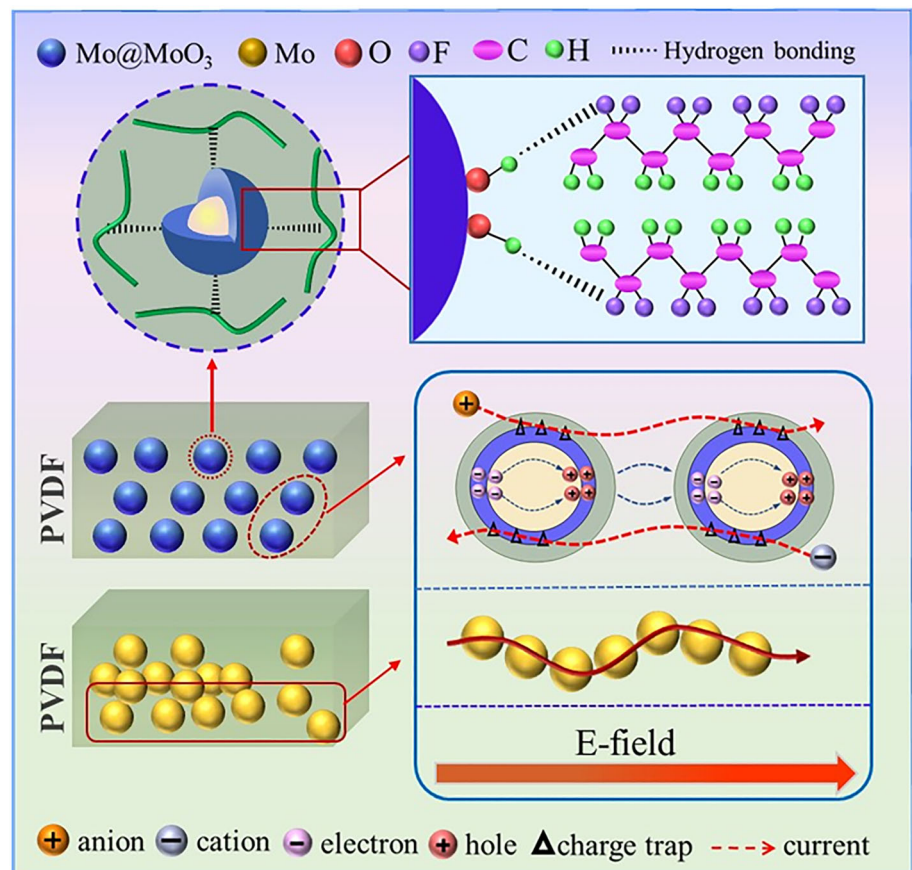
The above results suggest that the MoO<sub>3</sub> shell on the surface of Mo particles can significantly restrain the tanδ, conductivity, and largely enhance the ε of PVDF. To better comprehend the role of the core–shell structured fillers in enhancing the dielectric properties of composites, a more visual schematic is

proposed and depicted in Fig. 9. Based on the SEM images, as indicated in Fig. 4, the Mo@MoO<sub>3</sub> particles show relatively homogeneous dispersion in the PVDF matrix compared with the raw Mo, attributive to the enhanced interface interaction from the presence of the MoO<sub>3</sub> interlayer. For Mo@MoO<sub>3</sub>/PVDF composites, the hydroxyl groups on the surface of the MoO<sub>3</sub> can interact with the F atoms in the PVDF chain to form hydrogen bonds, as indicated in Fig. 8, which strengthens the interfacial interactions and also facilitates the IP effects to a large extent. The homogeneous dispersion of filler in the matrix makes the distance between adjacent Mo particles longer than that for the inhomogeneous dispersion system. In the latter, the Mo particles easily aggregate to form particle cluster, thereby resulting in a low  $f_c$ ; whereas, in the former, the filler particles are separated from each other thanks to good even dispersion in the matrix, thus leading to a delayed  $f_c$ . Based on the TEM images, as indicated in Fig. 3b–c, e–f, the thickness of the MoO<sub>3</sub> shell on the surface of Mo is approximately 10 nm and 20 nm when Mo was calcined at 500 °C for 3 h and 600 °C for 3 h,

respectively, which can provide extensive trapping sites along the expanded interfaces, thus increasing the filler polarizations and suppressing the low-frequency charge transport owing to the interlayer' wide forbidden band. Through altering the calcination conditions such as temperature and time, the desirable crystal structure and optimal shell can be reached for the best dielectric properties of the composites. Recall from the previous description of  $\epsilon$  and  $\tan\delta$  in the Mo@MoO<sub>3</sub>/PVDF, the intermediately calcined Mo@MoO<sub>3</sub> fillers (like Mo-2) show the highest  $\epsilon$  and the lowest  $\tan\delta$ , confirming again that the improved dielectric properties of the calcined Mo/composites should be attributed to the particular core–shell structured filler morphology. Therefore, it is the MoO<sub>3</sub> interlayer that not only enhances the interfacial interactions resulting in good dispersion in the matrix, but also effectively blocks long range charge migration thereby markedly constraining the leakage current and loss to very low levels of the Mo@MoO<sub>3</sub>/PVDF composites.

Figure 9 plots the Cole–Cole curves of the permittivity imaginary part ( $\epsilon''$ ) versus the permittivity real

**Fig. 8** The schematic diagram showing the mechanism for the effects of the interlayer on the interfacial interactions and dielectric properties of composites



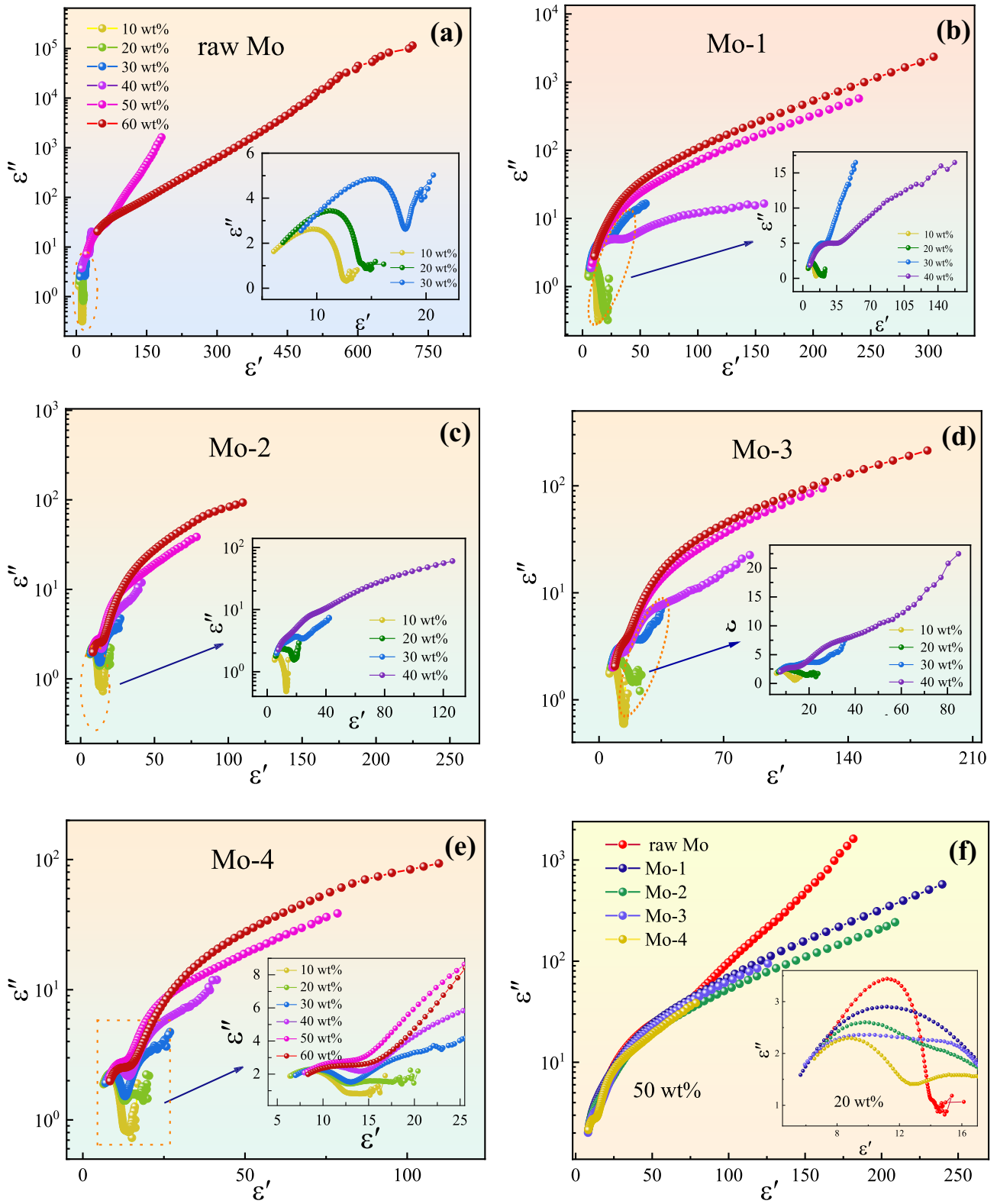


**Fig. 9** Plots the Cole–Cole curves of the permittivity imaginary part ( $\epsilon''$ ) versus the permittivity real part ( $\epsilon'$ ) for the PVDF filled with raw Mo and four types of Mo@MoO<sub>3</sub> with various loadings

part ( $\epsilon'$ ) for the PVDF filled with raw Mo and four types of Mo@MoO<sub>3</sub> with various loadings. It is obvious that all samples have two identical semicircle, representing two different relaxation mechanisms [37, 38]. The first small semicircle is related to the relaxation mechanism existing at the active interface of dipole polarization of the PVDF correlative with Debye model at high frequency, whereas, the second large semicircle can be interpreted as the IP in fillers/PVDF with non-Debye model at low frequency. It is well known that the polymer composites at a certain frequency does not follow the theory of monochromatic dispersion, so,  $\epsilon$  and  $\tan\delta$  are fitted into a Cole–Cole plot determined by the following equations:

$$\tan\delta = \frac{\epsilon''}{\epsilon'} \quad (4)$$

$$\epsilon^* = \epsilon_\infty + \frac{\epsilon_0 - \epsilon_\infty}{1 + i\omega\tau} - i\frac{\gamma}{\omega} \quad (5)$$

in which  $\epsilon_0$  and  $\epsilon_\infty$  are the low- and high-frequency permittivity,  $\tau$  is the relaxation time,  $\omega = 2\pi f$  is the angular frequency, and  $\gamma$  is the electric conductivity.

According to Eqs. (4–5), we know that the conductivity does influence the  $\epsilon''$ . So, in the second semicircle, the DC conductivity affects the actual graph' shape which deviates from the semicircle more significantly due to the presence of leakage current. The larger the leakage current is, the more remarkable the deviation is.

From Fig. 9a–e, as the filler loading increases from 10 to 60 wt%, the diameter of semicircle begins to increase, manifesting increased conductivity of the composites. And a gradual shift of the relaxation peak at low frequencies indicates gradually increased electric conductivity tendency for all composites and almost same relaxation process resulting from the polarization of C–F dipoles in PVDF and less loss relaxation response at high frequency. Compared with pristine Mo, the Mo@MoO<sub>3</sub>/PVDF exhibit much suppressed relaxation curve and obviously lower diameter of semicircle at low frequencies due to the presence of the MoO<sub>3</sub> interlayer. Moreover, as the shell thickness increases, the IP and relaxation related with conduction loss have been further suppressed at both low and high frequencies. As summarized in Fig. 9f, an obvious deviation from the second arc can be observed by comparing the composites with 20 wt% and 50 wt% of fillers, and the reason is attributed to the large discrepancy in conductivity for various composites due to

the variation in conductivities of filler by changing the calcining conditions.

## 4 Conclusion

Core–shell structured Mo@MoO<sub>3</sub> particles were prepared via a facile thermal oxidation technology under air at high temperature. The FT-IR, XRD, TGA and TEM measurements identify that the MoO<sub>3</sub> shell was successfully coated on the surface of Mo core. The Mo@MoO<sub>3</sub> particles show relatively homogeneous dispersion in the PVDF matrix due to the formation of hydrogen bond. Compared with the Mo/PVDF composites, the formation of a semi-conductive MoO<sub>3</sub> shell not only enhances the interfacial interactions promoting the homogeneous dispersion of fillers in the matrix, but also efficiently suppresses the  $\tan\delta$  through restraining leakage current. The remarkably suppressed  $\tan\delta$  is due to the presence of the crystalline MoO<sub>3</sub> interlayer, which prevents the Mo particles from touching with each other, and frustrates the formation of a conductive network in the matrix. Of particularly, with increasing the shell' thickness, the dielectric loss and conductivity of composites further declines. Therefore, the optimum dielectric properties of the composites can be reached by delicately designing and preparing the MoO<sub>3</sub> interlayer with controlled morphology. The obtained Mo@MoO<sub>3</sub>/PVDF composites with a high  $\epsilon$  but low  $\tan\delta$  have potential applications in microelectronics and electrical energy storage industry.

## Author contributions

All authors contributed to the study conception and design. WZ, TL, JZ and TY participated in the material preparation, data collection and analysis. WZ, DZ and WP carried out the study and collected important background information. Characterization and related discussion were performed by HW, XZ, JL and JL. Funding acquisition and Project administration were performed by WZ, DZ. The first draft of the manuscript was written by WP and all authors commented on previous versions of the manuscript. All authors have read and approved the final manuscript.



## Funding

The authors gratefully acknowledge the financial supports from the National Natural Science Foundation of China (No. 51937007), Shaanxi Provincial Natural Science Foundation, China (No. 2022JM-186), and acknowledge the Analytic Instrumentation Center of XUST.

## Data availability

All data generated or analyzed during this study are included in this published article.

## Declarations

**Conflict of interest** The authors have no relevant financial or non-financial interests to disclose. The authors have no conflicts of interest to declare that are relevant to the content of this article. All authors certify that they have no affiliations with or involvement in any organization or entity with any financial interest or non-financial interest in the subject matter or materials discussed in this manuscript. The authors have no financial or proprietary interests in any material discussed in this article. Authors are responsible for correctness of the statements provided in the manuscript. See also Authorship Principles. The Editor-in-Chief reserves the right to reject submissions that do not meet the guidelines described in this section.

**Supplementary Information:** The online version contains supplementary material available at <http://doi.org/10.1007/s10854-022-08393-5>.

## References

- H. Luo, C. Ma, X.F. Zhou, S. Chen, D. Zhang, Interfacial design in dielectric nanocomposite using liquid crystalline polymer. *Macromolecules* **50**(13), 5132–5137 (2017)
- H. Luo, X.F. Zhou, C. Ellingford, Y. Zhang, S. Chen, H.C. Zhou, D. Zhang, C.R. Bowen, C.Y. Wan, Interface design for high energy density polymer nanocomposites. *Chem. Soc. Rev.* **48**(16), 4424–4465 (2019)
- W.Y. Zhou, Y.J. Kou, M.X. Yuan, B. Li, H.W. Cai, Z. Li, F.X. Chen, X.R. Liu, G.H. Wang, Q.G. Chen, Z.M. Dang, Polymer composites filled with core@double-shell structured fillers: effects of multiple shells on dielectric and thermal properties. *Compos. Sci. Technol.* **181**, 107686 (2019)
- X. Xie, C. Yang, X.D. Qi, J.H. Yang, Z.W. Zhou, Y. Wang, Constructing polymeric interlayer with dual effects toward high dielectric constant and low dielectric loss. *Chem. Eng. J.* **366**, 378–389 (2019)
- M. Yuan, B. Li, S. Zhang, R. Rajagopalan, M.T. Lanagan, Thermally-stable low-loss polymer dielectrics enabled by attaching crosslinkable antioxidant to polypropylene. *ACS Appl. Polym. Mater.* **2**(3), 1356–1368 (2020)
- W.Y. Zhou, Y. Zhang, J.J. Wang, H. Li, W.H. Xu, B. Li, L.Q. Chen, Q. Wang, Lightweight porous polystyrene with high thermal conductivity by constructing 3D interconnected network of boron nitride nanosheets. *ACS Appl. Mater. Interfaces* **12**(41), 46767–46778 (2020)
- P. Wang, X.M. Zhang, W. Duan, W. Teng, Y.B. Liu, Q. Xie, Superhydrophobic flexible supercapacitors formed by integrating hydrogel with functional carbon nanomaterials. *Chin. J. Chem.* **39**(5), 1153–1158 (2021)
- Z.D. Wang, G.D. Meng, L.L. Wang, L.L. Tian, S.Y. Chen, G.L. Wu, B.K. Bo, Y.H. Cheng, Simultaneously enhanced dielectric properties and through plane thermal conductivity of epoxy composites with alumina and boron nitride nanosheets. *Sci. Rep.* **11**(1), 1–11 (2021)
- Z.D. Wang, X.Z. Wang, S.L. Wang, J.Y. He, T. Zhang, J. Wang, G.L. Wu, Simultaneously enhanced thermal conductivity and dielectric breakdown strength in sandwich AlN/Epoxy composites. *Nanomaterials* **11**(8), 1898 (2021)
- J.W. Zha, M.S. Zheng, B.H. Fan, Z.M. Dang, Polymer-based dielectrics with high permittivity for electric energy storage: a review. *Nano Energy* **89**, 106438–1–20 (2021)
- S.H. Kim, H.S. Kang, E.H. Sohn, B.J. Chang, I.J. Park, S.G. Lee, Analyses of low-temperature transport and thermoelectric properties of polycrystalline undoped n-ZrNiSn. *ACS Appl. Energy Mater.* **3**(9), 8937–8945 (2020)
- J.H. Ren, Z.Y. Wang, P. Xu, C. Wang, F. Gao, D.C. Zhao, S.P. Liu, H. Yang, D. Wang, C.M. Niu, Y.S. Zhu, Y.T. Wu, X. Liu, Z.L. Wang, Y. Zhang, Porous Co<sub>2</sub>VO<sub>4</sub> nano diskasa high energy and fast-charging anode fortieth um-ion batteries. *Nano-Micro Lett.* **14**, 5 (2022)
- J.W. Ren, Q.H. Li, L. Yan, L.H. Jia, X.H. Huang, L.H. Zhao, Q.H. Ran, M.L. Fu, Enhanced thermal conductivity of epoxy composites by introducing graphene@boron nitride nanosheets hybrid nanoparticles. *Mater. Des.* **191**, 108663 (2020)
- L.H. Zhao, L. Yan, C.G. Wei, Q.H. Li, X.L. Huang, Z.L. Wang, M.L. Fu, J.W. Ren, Synergistic enhanced thermal conductivity of epoxy composites with boron nitride nanosheets and microspheres. *J. Phys. Chem. C* **124**(23), 12723–12733 (2020)
- L.H. Zhao, C.J. Liao, Y. Liu, X.L. Huang, W.J. Ning, Z. Wang, L.C. Jia, J.W. Ren, A combination of aramid nanofiber and silver nanoparticle decorated boron nitride for the

- preparation of a composite film with superior thermally conductive performance. *Compos. Interfaces* **29**, 447–463 (2021)
16. L.C. Jia, Y.F. Jin, J.W. Ren, L.H. Zhao, D.X. Yan, Z.M. Li, Highly thermally conductive liquid metal-based composites with superior thermostability for thermal management. *J. Mater. Chem. C* **9**(8), 2904–2911 (2021)
  17. G.R. Chen, X. Wang, J.Q. Lin, W.L. Yang, H.D. Li, Y.N. Wen, L.D. Li, Z.C. Jiang, Q.Q. Lei, Nano-KTN@Ag/PVDF composite films with high permittivity and low dielectric loss by introduction of designed KTN/Ag core/shell nanoparticles. *J. Mater. Chem. C* **4**(34), 8070–8076 (2016)
  18. X. Lu, W. Deng, J.D. Wei, Y.H. Wan, J.J. Zhang, L. Zhang, L. Jin, Z.Y. Cheng, Crystallization behaviors and related dielectric properties of semicrystalline matrix in polymer-ceramic nanocomposites. *Compos. B. Eng.* **224**, 109195 (2021)
  19. B. Li, P.I. Xidas, K.S. Triantafyllidis, E. Manias, Effect of crystal orientation and nanofiller alignment on dielectric breakdown of polyethylene/montmorillonite nanocomposites. *Appl. Phys. Lett.* **111**(8), 082906 (2017)
  20. B. Li, M.X. Yuan, S.H. Zhang, R. Ramakrishnan, T.L. Michael, Abnormal high voltage resistivity of polyvinylidene fluoride and implications for applications in high energy density film capacitors. *Appl. Phys. Lett.* **113**(19), 193903 (2018)
  21. B. Li, G.F. Salcedo, P.I. Xidas, E. Manias, Improving electrical breakdown strength of polymer nanocomposites by tailoring hybrid-filler structure for high-voltage dielectric applications. *ACS Appl. Nano Mater.* **1**(9), 4401–4407 (2018)
  22. B. Li, P.I. Xidas, E. Manias, High breakdown strength polymer nanocomposites based on the synergy of nanofiller orientation and crystal orientation for insulation and dielectric applications. *ACS Appl. Nano Mater.* **1**(7), 3520–3530 (2018)
  23. Y.J. Kou, W.Y. Zhou, X. Li, Z.J. Wang, Y. Li, H.W. Cai, D.F. Liu, F.X. Chen, G.H. Wang, Z.M. Dang, Surface modification of GO by PDA for dielectric material with well-suppressed dielectric loss. *High Perf. Polym.* **31**(6), 1183–1194 (2019)
  24. T. Li, W.Y. Zhou, Y. Li, D. Cao, Y. Wang, G.Z. Cao, X.R. Liu, H.W. Cai, Z.M. Dang, Synergy improvement of dielectric properties and thermal conductivity in PVDF composites with core-shell structured Ni@SiO<sub>2</sub>. *J. Mater. Sci. Mater. Electron.* **32**(4), 4076–4089 (2021)
  25. W.Y. Zhou, T. Li, M.X. Yuan, B. Li, S.L. Zhong, Z. Li, X.R. Liu, J.J. Zhou, Y. Wang, H.W. Cai, Z.M. Dang, Decoupling of inter-particle polarization and intra-particle polarization in core-shell structured nanocomposites towards improved dielectric performance. *Energy Storage Mater.* **42**, 1–11 (2021)
  26. J.W. Zha, S.C. Yao, Y. Qiu, M.H. Zheng, Z.M. Dang, Enhanced dielectric properties and energy storage of the sandwich-structured poly(vinylidene fluoride-cohexafluoropropylene) composite films with functional BaTiO<sub>3</sub>@Al<sub>2</sub>O<sub>3</sub> nanofibres. *IET Nanodielectr.* **2**(3), 103–108 (2019)
  27. X. Lu, L. Zhang, Y. Tong, Z.Y. Cheng, BST-P(VDF-CTFE) nanocomposite films with high dielectric constant, low dielectric loss, and high energy-storage density. *Compos. B. Eng.* **168**, 34–43 (2019)
  28. X. Lu, X.W. Zou, J.L. Shen, L. Zhang, L. Jin, Z.Y. Cheng, High energy density with ultrahigh discharging efficiency obtained in ceramic-polymer nanocomposites using a non-ferroelectric polar polymer as matrix. *Nano Energy* **70**, 104551 (2020)
  29. Y.C. Li, X.Q. Bi, S.S. Wang, Y.H. Zhan, H.Y. Liu, Y.W. Mai, C.Z. Liao, Z.G. Lu, Y.Z. Liao, Core-shell structured polyethylene glycol functionalized graphene for energy-storage polymer dielectrics: combined mechanical and dielectric performances. *Compos. Sci. Technol.* **199**, 108341 (2020)
  30. D.Y. Shen, M.J. Wang, Y.M. Wu, Z.D. Liu, Y. Cao, T. Wang, X.F. Wu, Q.T. Shi, K.W. Chee, W. Dai, H. Bai, D. Dai, J.L. Lyu, N. Jiang, C.T. Lin, J.H. Yu, Enhanced thermal conductivity of epoxy composites with core-shell SiC@SiO<sub>2</sub> nanowires. *High Voltage* **2**(3), 154–160 (2017)
  31. S.L. Zhong, Z.M. Dang, W.Y. Zhou, H.W. Cai, Past and future on nanodielectrics. *IET Nanobiotechnol.* **1**(1), 41–47 (2018)
  32. W.Y. Zhou, F. Zhang, M.X. Yuan, B. Li, J.D. Peng, Y.Q. Lv, H.W. Cai, X.R. Liu, Q.G. Chen, Z.M. Dang, Improved dielectric properties and thermal conductivity of PVDF composites filled with core-shell structured Cu@CuO particles. *J. Mater. Sci.: Mater. Electron.* **30**(20), 18350–18361 (2019)
  33. W.Y. Zhou, X. Li, F. Zhang, C.H. Zhang, Z. Li, F.X. Chen, H.W. Cai, X.R. Liu, Q.G. Chen, Z.M. Dang, Concurrently enhanced dielectric properties and thermal conductivity in PVDF composites with core-shell structured  $\beta$ -SiC<sub>w</sub>@SiO<sub>2</sub> whiskers. *Compos. Part A Appl. Sci. Manuf.* **137**, 106021 (2020)
  34. W.Y. Zhou, Y. Gong, L.T. Tu, X. Li, W. Zhao, J.T. Cai, Y.T. Zhang, A.N. Zhou, Dielectric properties and thermal conductivity of core-shell structured Ni@NiO/poly(vinylidene fluoride) composites. *Alloys Compd.* **693**, 1–8 (2017)
  35. S.K. Abdel-Aal, M.F. Kandeel, A.F. El-Sherif, A.S. Abdel-Rahman, Synthesis, characterization, and optical properties of new organic-inorganic hybrid perovskites [(NH<sub>3</sub>)<sub>2</sub>(CH<sub>2</sub>)<sub>3</sub>]CuCl<sub>4</sub> and [(NH<sub>3</sub>)<sub>2</sub>(CH<sub>2</sub>)<sub>4</sub>]CuCl<sub>2</sub>Br<sub>2</sub>. *Phys. Status Solidi A* **2100036**, 1–9 (2021)
  36. J.Y. Li, K. McPhedran, E. Szalinska, A.M. McLeod, S.P. Bhavsar, J. Bohr, A. Grgicak-Mannion, K. Drouillard, Characterizing polychlorinated biphenyl exposure pathways from sediment and water in aquatic life using a food web

- bioaccumulation model. *Integr. Environ. Assess. Manag.* **398–411**, 1–14 (2019)
37. A.S. Abouhaswa, T.A. Taha, Tailoring the optical and dielectric properties of PVC/CuO nanocomposites. *Polym. Bull.* **77(11)**, 6005–6016 (2020)
38. S.S. El-Khiyami, R.S. Hafez, Dielectric study and Cole-Cole plots of poly(methyl methacrylate) doped with nanostructured metal oxides. *J. Polym. Res* **28(10)**, 1–19 (2021)

**Publisher's Note** Springer Nature remains neutral with regard to jurisdictional claims in published maps and institutional affiliations.